nature geoscience

SUPPLEMENTARY INFORMATION

DOI: 10.1038/NGEO2731

Southern Ocean warming delayed by circumpolar upwelling and equatorward transport

Kyle C. Armour[1], John Marshall[2], Jeffery R. Scott[2,3], Aaron Donohoe[4] and Emily R. Newsom[5]

[1] *School of Oceanography and Department of Atmospheric Sciences, University of Washington, Seattle, WA 98195*
[2] *Department of Earth, Atmospheric and Planetary Sciences, Massachusetts Institute of Technology, Cambridge, MA 02139*
[3] *Center for Global Change Science, Massachusetts Institute of Technology, Cambridge, MA 02139*
[4] *Polar Science Center, Applied Physics Laboratory, University of Washington, Seattle, WA 98195*
[5] *Department of Earth and Space Sciences, University of Washington, Seattle, WA 98195*

This document contains the following supplementary material:

(i) Observed Southern Ocean sea-surface temperature trends over 1950-2012 (Fig. S1).

(ii) Additional details of the ocean temperature and heat content trend analysis reported in the main text; a comparison of results from different choices of ocean temperature bias corrections and subsurface temperature data sets; a comparison of thermosteric sea-level trends derived from observed ocean warming to those measured by satellite altimetry; and a comparison of results from different ocean reanalyses (Figs. S2-S4).

(iii) Additional details of the sea-surface heat flux analysis reported in the main text; a discussion of the relationship between surface heat flux trends and changing air-sea temperature gradients; and a comparison of results from different surface heat flux data sets (Figs. S5-S7).

(iv) An analysis of internal variability in the CMIP5 pre-industrial control simulations (Figs. S8-S9).

(v) Additional information about and supplementary results of the ocean-only MITgcm simulations (Figs. S10-S14).

(i) Southern Ocean sea-surface temperature trend over 1950-2012

Figure S1 shows the 1950-2012 linear sea-surface temperature (SST) trend calculated from the National Oceanic and Atmospheric Administration's (NOAA) Extended Reconstruction Sea-Surface Temperature (ERSST) data set[1]. Over this period, global SST increased at $0.08°$/decade, while south of 50°S increased by only $0.02°$/decade.

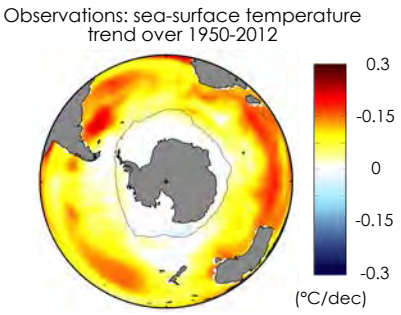

Figure S1. Observed trends in annual mean sea-surface temperature over 1950-2012. Calculated from NOAA's ERSST data set. Grey lines show maximum winter sea-ice extent, as in Fig. 1 of the main text.

(ii) Southern Hemispheric ocean potential temperature and heat content trends

Comparison of different observational data sets. The depth-integrated heat storage trends shown in the main text (Fig. 1d) are derived from two objectively-analyzed subsurface temperature data sets. The first is the Met Office Hadley Centre's Objectively Analyzed EN4 (version 1.1) data set[2], shown again here in Fig. S2. Ocean temperature corrections have been made by ref. 2 to adjust for time-varying biases in mechanical bathythermograph (MBT) and expendable bathythermograph (XBT) profiles following the methods of Gourestki and Reseghetti (2010) (ref. 3); we hereafter refers to this data set as EN4 (G). We calculate the Southern Hemispheric (SH) mean ocean heat storage as a linear trend in total hemispheric heat content over 1982-2012, giving 0.57 Wm^{-2} for EN4 (G).

For comparison, ref. 2 also provides objectively analyzed ocean temperatures that have been derived following the bias correction methods of Levitus et al (2009) (ref. 4); we hereafter refer to this data set as EN4 (L). Results using EN4 (L) and EN4 (G) are visually indistinguishable (Fig. S2c). The SH mean heat storage over 1982-2012 is 0.56 Wm^{-2} for EN4 (L). For this reason, we only show EN4 (G) in the main text.

The second subsurface temperature data set shown in the main text (Fig. 1c) is that of Ishii et al. (2009) (ref. 5). While Ishii et al. only provide temperature fields to a depth of 1500 m, the zonal-mean ocean potential temperature and heat storage trends are in good agreement with those of EN4 (G), with maximum warming in the vicinity of the Antarctic Circumpolar Current (ACC) and less warming to the south (Fig. S2). The SH mean ocean heat storage averaged over 1982-2012 is 0.41 Wm^{-2} for the Ishii data set. The SH heat storage trend results for the observational products are summarized in Table 1.

Comparison of EN4 to satellite altimetry measurements of sea-surface height trends. It is perhaps not surprising that the EN4 and Ishii data sets produce such similar patterns of ocean warming, given that they are derived from a similar set of subsurface ocean temperature measurements. One limitation of these data sets is that observations were sparse throughout the SO prior to the advent of the network of ARGO profiling floats in the early 2000s – particularly south of the ACC and below 1500 m. However, an independent evaluation of the observed ocean warming trends can be achieved using satellite altimetry measurements of sea-surface height changes changes. Sea-surface height (SSH) trends over 1993-2012 from the AVISO altimetry product (http://www.aviso.altimetry.fr/) is shown in Figs. S3b,c. Note that all SSH trends are calculated here as anomalies from the global mean trend, thus removing trends in global ocean mass and allowing for a comparison between satellite observations of SSH and the SSH changes implied by ocean warming. We calculate the patterns of thermosteric SSH trends from the EN4 (G) ocean temperature trends over 1993-2012 as

$$\frac{d\mathrm{SSH}}{dt} = \int_{\mathrm{bottom}}^{\mathrm{surface}} \alpha(z) \frac{d\theta(z)}{dt} dz, \tag{1}$$

where α is the thermal expansion of sea water calculated from to the Gibbs Seawater Oceanographic Toolbox (ref. 6), and θ is ocean potential temperature. There are some differences between the regional patterns of SSH trends estimated from EN4 (G) and measured from AVISO, likely owing to halosteric and mass redistribution effects not included in our EN4 (G) estimate. However, they show broad agreement with one another, and particularly in the zonal mean, with the highest rates of SSH increase in the vicinity of the ACC and the lowest rates to the south of the ACC (Fig. S3). These results are consistent with refs. 7-9 that find that patterns of sea-level rise in the Southern Hemisphere can be largely attributed to thermosteric effects associated with ocean heat uptake and storage.

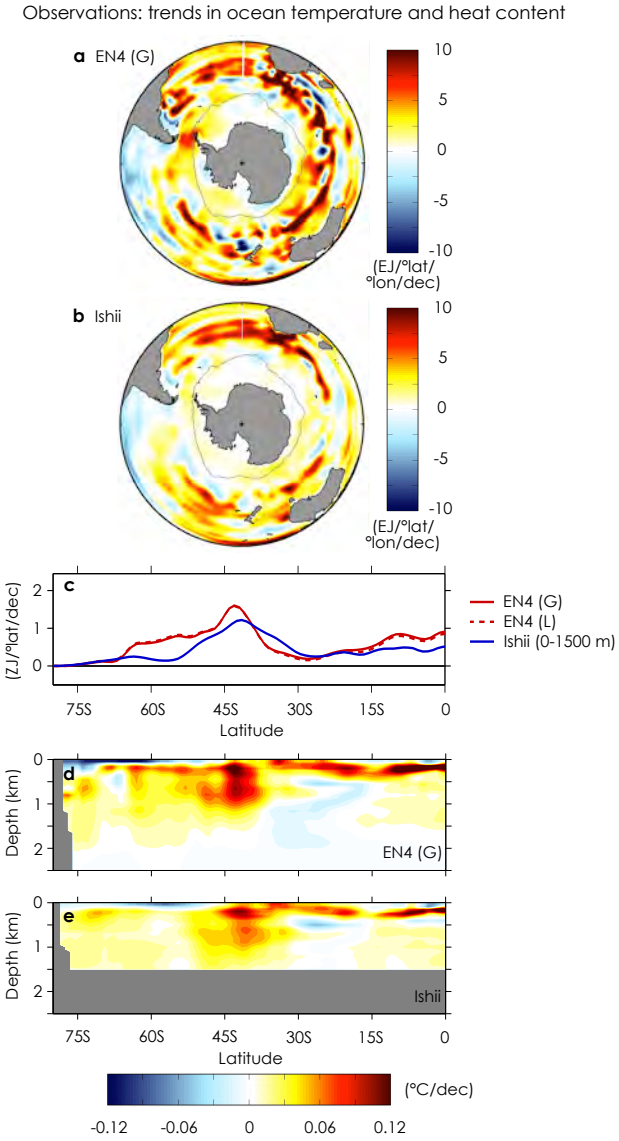

Figure S2. Observed trends in annual-mean depth-integrated ocean heat content and zonal mean ocean potential temperature over 1982-2012. a, EN4 (G) depth-integrated heat content trend; **b,** Ishii depth-integrated heat content trend; **c,** Zonally and depth integrated heat content trends; **d,** EN4 (G) zonal-mean ocean potential temperature trend; **e,** Ishii zonal-mean ocean potential temperature trend. Grey lines show maximum winter sea-ice extent, as in Fig. 1 of the main text.

Comparison of EN4 to ocean reanalyses. To further assess the plausible range of SO temperature and heat content trends, we can compare the EN4 (G) observations to the results of several different ocean reanalyses, which assimilate ocean temperature and satellite altimetry data to produce dynamically consistent estimates of historical ocean changes. In particular, we consider: the CMCC Global Ocean Physical Reanalysis System (C-GLORS; ref. 10); the ECMWF Ocean Reanalysis System 4 (ORAS4; ref. 11); the Simple Ocean Data Assimilation (SODA; ref. 12); and the University of Hamburg contribution of the Estimating the Circulation and Climate of the Ocean project (GECCO2; ref. 13).

There is a broad range of simulated warming trends across the ocean reanalyses (Fig. S4), with several reanalyses (C-GLORS, ORAS4, SODA) showing less warming than EN4 (G), or even cooling, south of the ACC, and with one reanalysis (GECCO2) showing more warming than EN4 (G) near Antarctica. Yet, every ocean reanalysis shows maximum warming and depth-integrated heat storage in the vicinity of the ACC. This pattern of maximum heat storage within the vicinity of the ACC, and reduced heat storage to the south, is thus robust across ocean temperature data sets, satellite altimetry observations of SSH trends, ocean reanalyses, and the CMIP5 historical simulation results reported in the main text.

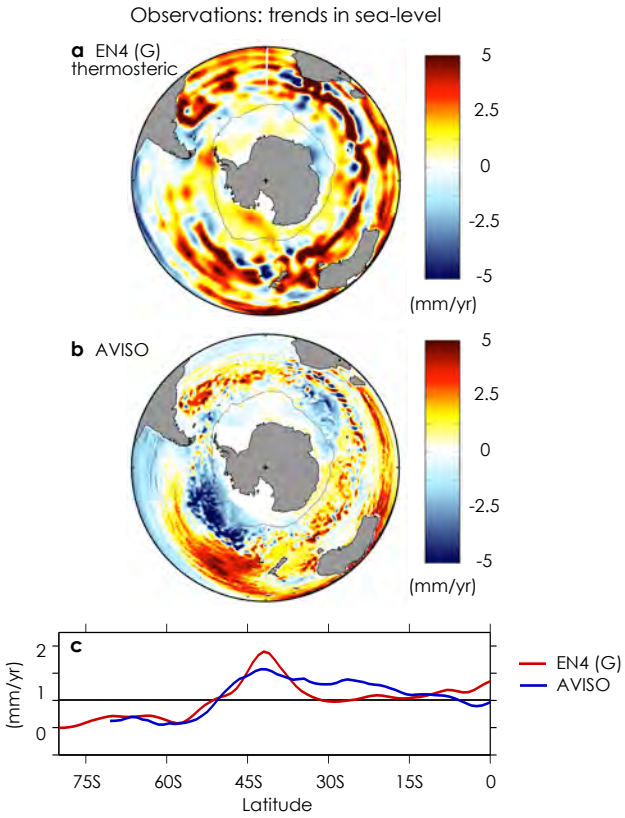

Figure S3. Annual mean sea-surface height trends over 1993-2012. **a,** Thermosteric sea-surface height trend derived from EN4 (G); **b,** Sea-surface height trend measured from AVISO satellite altimetry. Each are shown as anomalies from global mean trends. Grey lines show maximum winter sea-ice extent, as in Fig. 1 of the main text.

We further calculate SH mean ocean heat content trends over 1982-2012 for each of the ocean reanalysis products (Table 1). They show generally good agreement with the heat storage calculated observational data sets described above. Taken altogether, the observations and ocean reanalyses suggest a SH heat storage of about 0.4-0.6 Wm^{-2} over 1982-2012, which is the range that we report in the main text.

Observational/Reanalysis Product	SH heat storage (Wm^{-2})
EN4 (G)	0.57
EN4 (L)	0.56
Ishii	0.41
C-GLORS	0.26
ORAS4	0.48
SODA	0.63
GECCO2	0.53

Table 1. Southern Hemisphere mean heat content trends over 1982-2012.

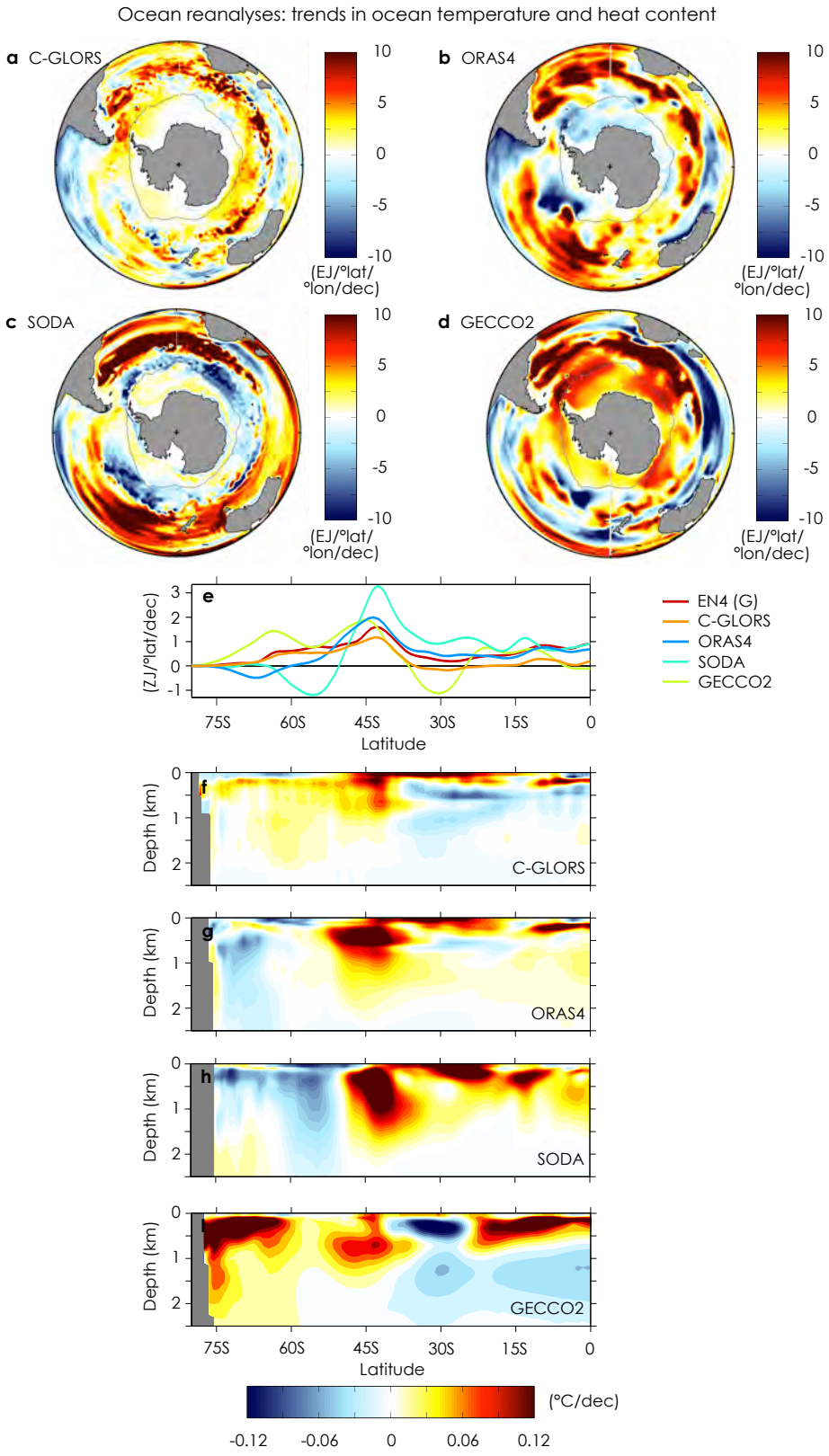

Figure S4. Trends in depth-integrated ocean heat content and zonal mean ocean potential temperature from ocean reanalyses a-d, Depth-integrated heat content trends; **e,** Zonally and depth integrated heat content trends; **f-i,** Zonal-mean of ocean potential temperature trends. Grey lines show maximum winter sea-ice extent, as in Fig. 1 of the main text.

(iii) Sea-surface heat flux trends

Radiative and turbulent components of the net surface heat flux trend. The trend in annual-mean net sea-surface heat flux (SHF) over 1982-2012 used in the main text (Fig. 1b, shown again here as Fig. S5a) is calculated from the Objectively Analyzed air-sea Flux for the Global Oceans Project (OAFlux) data set[14]. The net SHF trend is calculated as the sum of (i) the linear trend in sensible and latent heat flux over this period (Fig. S5b), and (ii) an estimate of the linear trend in net shortwave (SW) and longwave (LW) surface radiation based on observations from the International Satellite Cloud Climatology Project (ISCCP)[15] (Fig. S5c). Surface SW and LW radiation from ref. 15 are only available over 1984-2009, so we take the trend over this period as an approximation of the trend over 1982-2012. Nearly all of the spatial structure in the net SHF trend comes from the turbulent (sensible and latent) heat fluxes (cf. Figs. S5a,b), and our results are not sensitive to the period used to estimate SW and LW radiation trends.

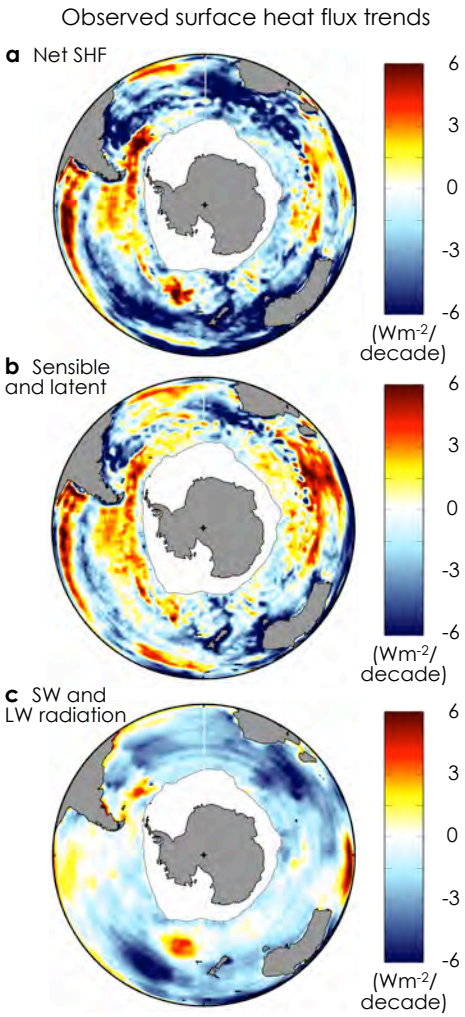

Figure S5. Observed trends in sea-surface heat flux. a, Annual-mean net sea-surface heat flux trend over 1982-2012 (positive into ocean); **b,** Net turbulent (sensible + latent) heat flux trend over 1982-2012; **c,** Net surface radiation flux (SW + LW) trend over 1984-2009. Grey lines show maximum winter sea-ice extent, as in Fig. 1 of the main text.

Relationship between turbulent heat flux trends and air-sea temperature gradient trends. The spatial pattern of SHF trends is predominantly set by trends in turbulent (sensible and latent) heat fluxes (Fig. S5). In turn, these turbulent heat fluxes reflect changes in air-sea temperature gradients. Figure S6 shows trends 2 m air temperature from the NOAA National Center for Environmental Predictions' Reanalysis-2 (NCEP2; ref. 16) over 1982-2012, compared with trends in sea-surface temperature from the Optimum Interpolation Sea-Surface Temperature (OISST; ref. 17) data set used in the main text. Note that NCEP2 and OISST are the same data sets employed by Yu et al. (ref. 14) to produce the OAFlux SHF product as well. We see that equatorward of the ACC the sea surface has warmed at a greater rate than near-surface air temperature, while

south of the ACC near-surface air temperature has warmed at a greater rate than the sea surface (Fig. S6). That is, the robust features of the SHF trends seen in Figs. 1b and S5 – with enhanced heat uptake south of the ACC and enhanced heat loss to the north – have been driven by these changing air-sea temperature gradients. SHFs thus act to damp the SST trends, which have been driven by changes in meridional ocean heat flux convergence as described in the main text.

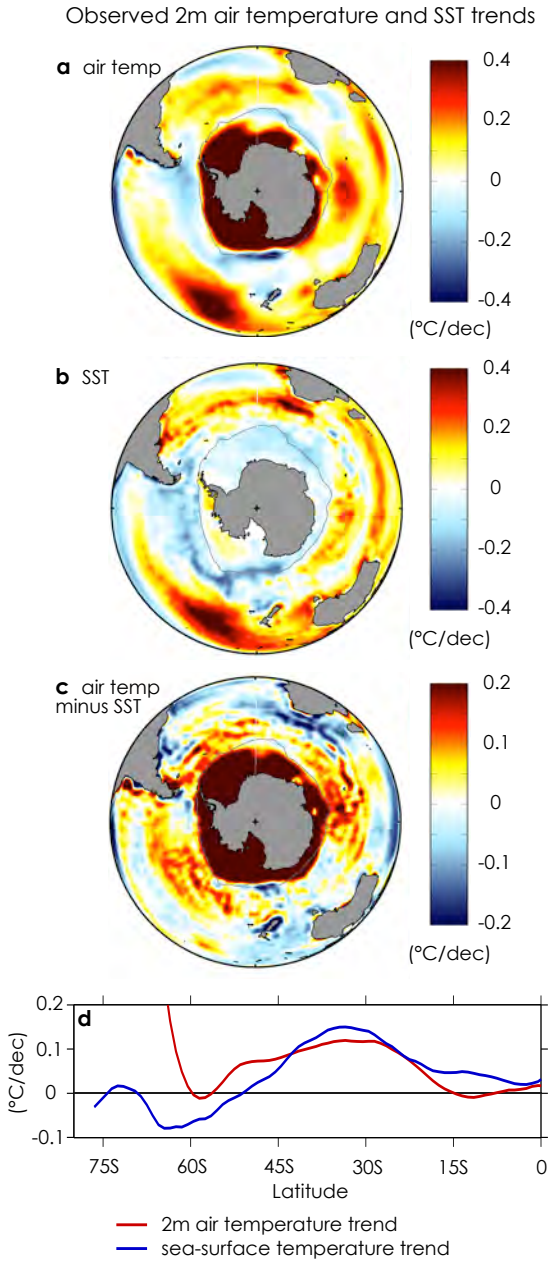

Figure S6. Observed trends in sea-surface temperature and near-surface air temperature over 1982-2012. **a,** Annual-mean 2 m air temperature trend from NCEP2; **b,** Annual-mean sea-surface temperature trend from OISST; **c,** Difference between 2 m air temperature and SST trends (positive when atmosphere warming faster); **d,** Zonal mean of 2 m air temperature and SST trends. Grey lines show maximum winter sea-ice extent, as in Fig. 1 of the main text.

Comparison of observational sea-surface heat flux data sets. Here we consider the robustness of the SHF trends over 1982-2012 (Fig. S5a). Uncertainties in surface heat fluxes are large, with the estimated monthly mean error around 5 Wm^{-2} for latent and sensible heat fluxes over the Southern Ocean[14]. However, the trends in surface heat fluxes reach values of

± 10 Wm^{-2}/decade over the Southern Ocean over the period 1982-2012 (Fig. S5), and thus the surface heat flux trends are statistically significant where they show the greatest changes.

We further compare the OAFlux SHF trends over 1982-2012 to those from two other observationally-derived data sets: the National Oceanography Centre Southampton (NOCS) Version 2.0 Surface Flux data set[18], an objectively analyzed data set that is derived from marine surface measurements of the International Comprehensive Ocean-Atmosphere Data Set (ICOADS[19]); and the Coordinated Ocean-ice Reference Experiment (CORE) 2 protocol[20]. Figure S7 shows that there is substantial spatial differences in SHF trends across these three data sets. However, they broadly agree with one another in the zonal mean, with each product showing enhanced heat loss to the atmosphere equatorward of the ACC and enhanced heat gain poleward of the ACC (Fig. S7d), as expected from the observed trends in air-sea temperature gradients (Fig. S6). While OAFlux and NOCS do not provide estimate of SHFs in the vicinity of sea ice, CORE2 shows enhanced surface heat gain in this region (Fig. S7b), consistent with the CMIP5 historical simulations reported in the main text (Fig. 2b).

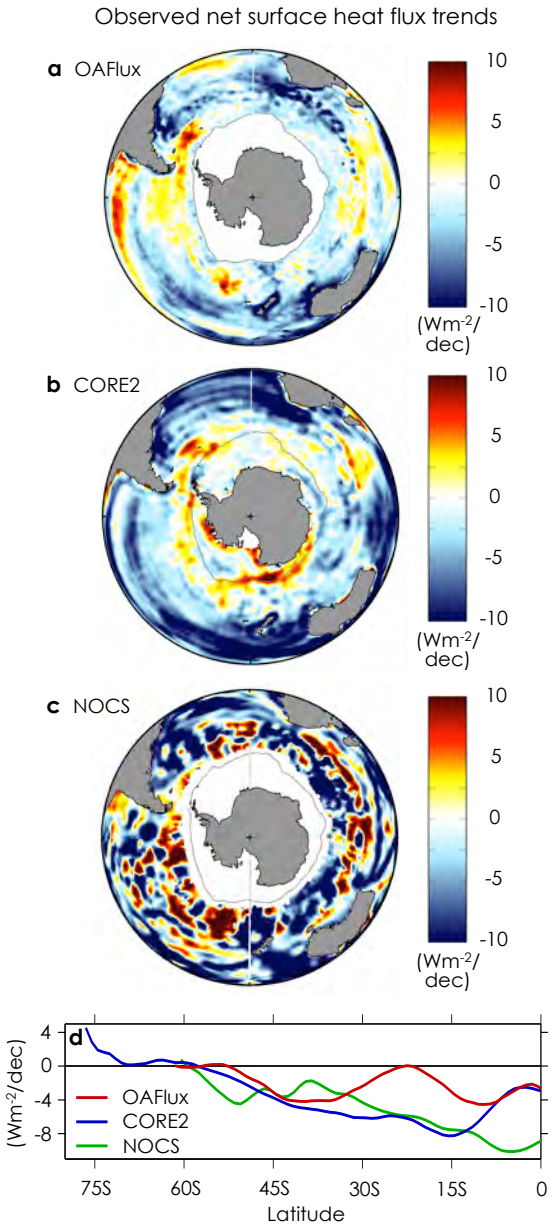

Figure S7. Observed trends in sea-surface heat flux over 1982-2012 for several different products (positive into ocean). a, OAFlux; **b,** CORE2; **c,** NOCS; and **d,** Zonal-mean sea-surface heat flux trends. Grey lines show maximum winter sea-ice extent, as in Fig. 1 of the main text.

(iv) Internal variability in the CMIP5 pre-industrial control simulations

Here we quantify the extent to which internal variability may be playing a role in delayed SO warming using the long pre-industrial control simulations of the same set of CMIP5 models used in the main text. Table 2 lists the models and the length of the simulations.

Model	Length of simulation (yrs)
ACCESS1-0	500
bcc-csm1-1	500
CCSM4	1051
CMCC-CM	330
CNRM-CM5	850
CSIRO-Mk3-6-0	500
EC-EARTH	452
GFDL-ESM2G	500
MIROC5	670
MPI-ESM-LR	1000
MRI-CGCM3	500
NorESM1-M	501

Table 2. CMIP5 models and length of pre-industrial control simulations.

Internal variability in delayed SO warming. To quantify the role of internal (i.e., unforced) variability in delayed SO warming over the historical period and within the CMIP5 abrupt CO_2 quadrupling simulations, we define a measure of delayed SO warming (D) to be the difference between the SST anomaly averaged south of 50°S and the global-mean SST anomaly. D has been observed[1] to change at a rate of -0.06°/decade over the 63-yr period 1950-2012 and -0.12°/decade over the 31-yr period 1982-2012, where the negative values signify that the SO has been slower to warm than the global ocean. We calculate the probability density of 63-yr and 31-yr trends in D within the pre-industrial control simulations of each model using a Moving Block Bootstrap method (with 10,000 trends in D drawn at random from each timeseries, with replacement). The results from all models are then averaged to produce a CMIP5-mean estimate of internal variability.

Figure S8a shows the internal variability in 31-yr trends in D compared to the observed and CMIP5-mean (i.e., forced) trends over 1982-2012. The observations (solid vertical line) lie outside the 95% (2.5-97.5%) confidence interval (blue shading), indicating that internal variability alone is insufficient to explain the degree of delayed SO warming observed over this period. Interestingly, the difference between the observed and CMIP5-mean trends in D (dashed vertical line) are well within the range of internal variability. Likewise, the observed 63-yr trend in D over 1950-2012 lies far outside the 95% confidence interval of internal variability in 63-yr trends within the CMIP5 control simulations (Fig. S8b). Moreover, the difference between the observed and CMIP5-mean trends in D over 1950-2012 are within the range of internal variability.

Figure S8c shows the probability density of 31-yr means in D within the pre-industrial control simulations, which can be directly compared to the 31-yr mean in D centered at year 100 following the abrupt quadrupling of CO_2 within the CMIP5 models (dashed vertical line). Altogether, we take these results as evidence that internal variability is insufficient to explain the degree of delayed SO warming in observations and CMIP5 simulations.

Internal variability in surface heat uptake, ocean heat storage, and northward ocean heat transport. Here we quantify the internal variability in zonal-mean surface heat uptake, ocean heat storage, and ocean heat transport within the CMIP5 pre-industrial control simulations. Using a Moving Block Bootstrap method (described above) we calculate each quantity over 31-yr periods for comparison with the historical simulations of the CMIP5 models over 1982-2012 (Figs. 2a-e of the main text), and over 100-yr periods for comparison with the abrupt CO_2 quadrupling simulations of the CMIP5 models (Figs. 2f-j of the main text). The shading in Fig. S9 shows the 95% (2.5-97.5%) confidence range in shading about the zonal-mean heat uptake, storage and transport anomalies. Over the historical period, heat uptake south of the ACC is well

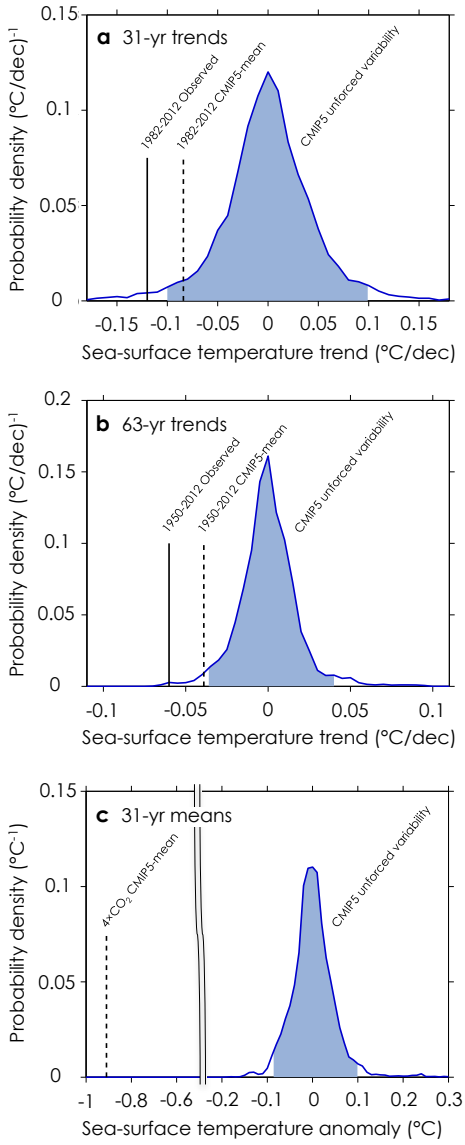

Figure S8. Internal variability in delayed SO warming in CMIP5 pre-industrial control simulations. a, 31-yr trends; **b,** 63-yr trends; and **c,** 31-yr means. Vertical lines show the observed and CMIP5-mean values of delayed SO warming over different periods. Blue shading shows 95% (2.5-97.5%) confidence intervals.

outside the range of internal variability, while ocean heat storage is sufficiently small to be within the range of internal variability; ocean heat transport changes are statistically significant everywhere. On 100-yr timescales, internal variability in heat uptake, storage and transport are small relative to the magnitude of changes seen following following abrupt CO_2 quadrupling. In all cases, the range of variability is smaller than the uncertainty range across CMIP5 models shown in Fig. 2 of the main text, which includes a combination of internal variability and the range of model response to forcing.

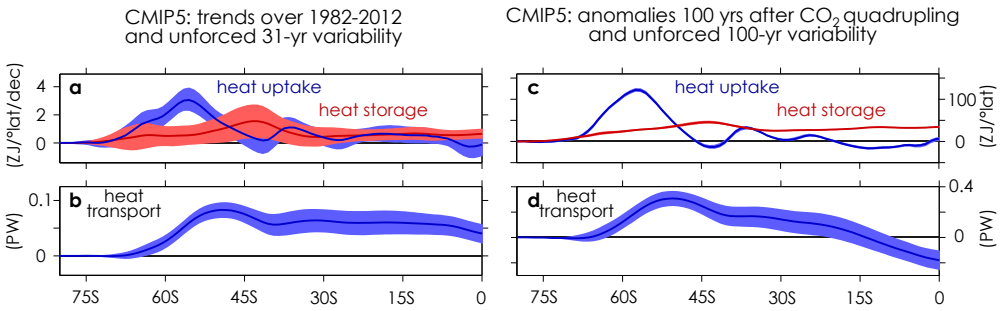

Figure S9. CMIP5-mean trends over 1982-2012 (left) and response to CO_2 forcing (right). a, Zonally integrated average sea-surface heat flux (blue) and full-depth ocean heat content trend (red); **b,** Anomalous OHT for CMIP5-mean (blue); **c,d,** As in **a,b**, but anomalies over 100 yrs in response to abrupt CO_2 quadrupling. Shading shows the 95% (2.5-97.5%) range of internal variability across the CMIP5 models.

(v) Ocean-only MITgcm simulations

Here we present supplementary diagnostics and results of additional forcing simulations performed with the MITgcm ocean-only model.

Meridional overturning circulation (MOC) changes under GHG forcing. Figure S8 shows the anomalous MOC at 100 years into the uniform GHG forcing simulation, and the anomalous temperature difference between the GHG and passive tracer simulations at that time. Changes in circulation are small everywhere south of the ACC, reflecting the fact that the high-latitude SO is stratified by salinity and relatively insensitive to changes in temperature. Differences between the GHG and passive tracer forcing simulations are similarly small, and mainly reflect a greater amount of heat trapped near the surface due to enhanced stratification under GHG forcing (absent in the the passive tracer scenario).

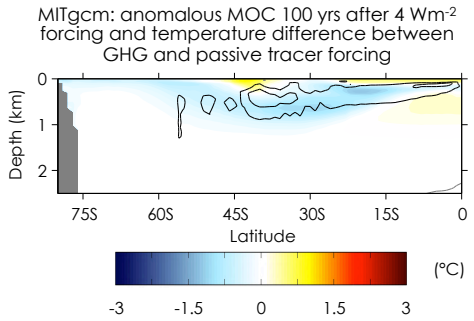

Figure S10. MITgcm MOC response to abrupt GHG forcing and temperature difference between GHG and passive tracer forcing scenarios. Difference in zonal-mean ocean potential temperature anomaly at year 100 between GHG and passive tracer forcing scenarios. Contours show the anomalous MOC (relative to the control) at year 100 of the GHG forcing scenario (black contours show positive circulation anomaly in 2 Sv increments, gray contours show negative circulation anomaly in -2 Sv increments).

Mixed layer response to GHG forcing. Figure S9 shows the change in wintertime (JJA) mixed layer depth over the SO (relative to the control) in the MITgcm 100 years into the uniform GHG forcing simulation. There is an overall shoaling of mixed layers in the vicinity of the mode water formation regions on the equatorward flank of the ACC, consistent with enhanced heat storage near the surface in those regions (Figs. 3a,e of the main text).

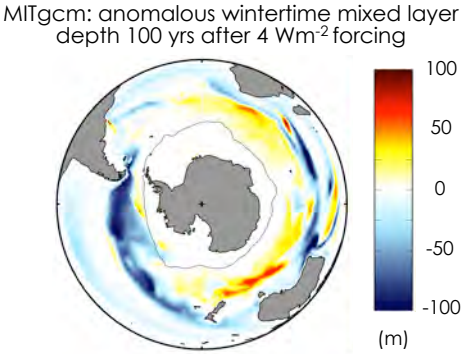

Figure S11. MITgcm wintertime (JJA) mixed layer depth response to abrupt GHG forcing. Mixed layer depth anomaly relative to the control at year 100 of the GHG forcing scenario described in the main text. Grey line shows maximum winter sea-ice extent, as in Fig. 1 of the main text.

MITgcm response to westerly wind forcing. Figure S12 shows the MITgcm response to an idealized, sustained westerly wind forcing. The pattern and magnitude of the applied zonal wind stress is based on a one standard deviation perturbation of the Southern Annular Mode (SAM) as calculated from the linearly detrended National Center for Environmental Prediction (NCEP) Global Ocean Assimilation System (GODAS) reanalysis[21] over 1980-2014. To mimic the observed trends that are associated with stratospheric ozone depletion, the wind stress pattern is multiplied by a spatially uniform factor that varies seasonally, peaking in late November, but scaled so that the annual-mean value matches one standard deviation of the SAM. The resulting wind stress is applied concurrently with the stored 'control' sea-surface buoyancy and momentum fluxes and the 1 $\mathrm{Wm}^{-2}\mathrm{K}^{-1}$ radiative feedback as described in the main text. See ref. 22 for additional details of the simulation. The initial effect of this strengthening and poleward shift of the westerly winds is cooling south of the ACC and warming to the north, driven by substantial changes in the MOC and OHT (Fig. S12a-c). However, after several decades the response becomes warming south of the ACC as the anomalous OHT diminishes and relatively warm water is upwelled from depth (Fig. S12d-f).

MITgcm response to freshwater forcing. While long-term changes in the SO hydrologic cycle are not well constrained by observations, ref. 23 find that within the CMIP5-mean, precipitation minus evaporation (P-E) averaged south of 50°S increases by about 2595 Gt/yr from pre-industrial to present, amounting to about a 10% increase over this period. They further note that this P-E change is an order of magnitude larger than the estimated current input of freshwater from changes in the Antarctic Ice Sheet. To evaluate the response of the SO to an enhanced hydrologic cycle, we apply forcing as an abrupt and sustained P-E anomaly averaged over the surface of the SO, everywhere 50°S, amounting to an increase of about 0.15 mm/day of freshwater input. As in the other MITgcm simulations, this forcing is applied concurrently with the stored 'control' sea-surface buoyancy and momentum fluxes and the 1 $\mathrm{Wm}^{-2}\mathrm{K}^{-1}$ radiative feedback as described in the main text.

Figure S13 shows the MITgcm response at following the freshwater forcing. Initially there is surface cooling and warming at depth around Antarctica (Fig. S13a-d), consistent with the freshening of the sea surface inhibiting deep convection and vertical mixing, thus decreasing the upward flux of heat from warmer waters at depth[??,??]. These anomalously fresh and cool surface waters are continuously advected equatorward by the background MOC (Fig. S13d,h) so that on multidecadal timescales the cooling and freshening signal extends northward beyond the ACC (Fig. S13e-h). This results in anomalous southward OHT across the ACC, by the same process that passive tracer and GHG forcing simulations result in anomalous northward OHT across the ACC when surface waters are warmed. The patterns seen in Fig. S13, with southward OHT across the ACC and a maximum cooling on the northern flank of the ACC, are consistent with the results of a similar freshwater forcing simulation performed within a CMIP5 GCM (ref. 23). Altogether, freshwater forcing results in only slightly more cooling south of the ACC than north of the ACC, and thus does not appear to play a primary role in delayed SO warming.

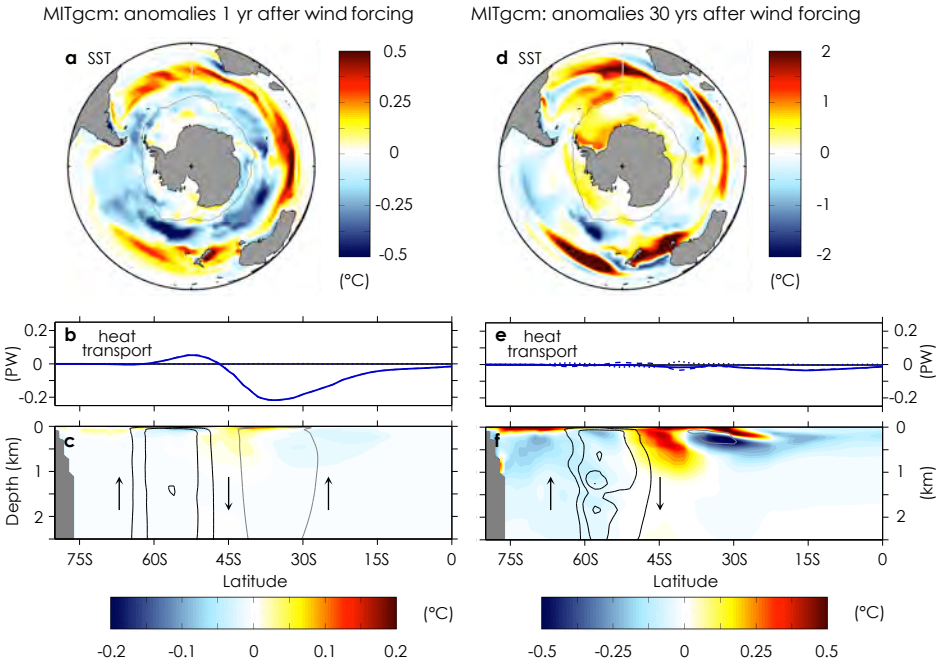

Figure S12. MITgcm response to abrupt wind forcing after 1 yr (left) and after 30 yrs (right). a, Annual-mean sea-surface temperature anomaly; **b,** Anomalous OHT (solid, dashed and dotted lines show total, residual-mean advection, and diffusion, respectively); **c,** Zonal-mean ocean potential temperature anomaly, with contours showing the anomalous MOC (relative to control; black contours show positive circulation anomaly in 2 Sv increments, gray contours show negative circulation anomaly in -2 Sv increments, and arrows show orientation of the anomalous circulation); **d-f,** As in **a-c**, but at yr 30. Grey line in **a** and **d** shows maximum winter sea-ice extent, as in Fig. 1 of the main text.

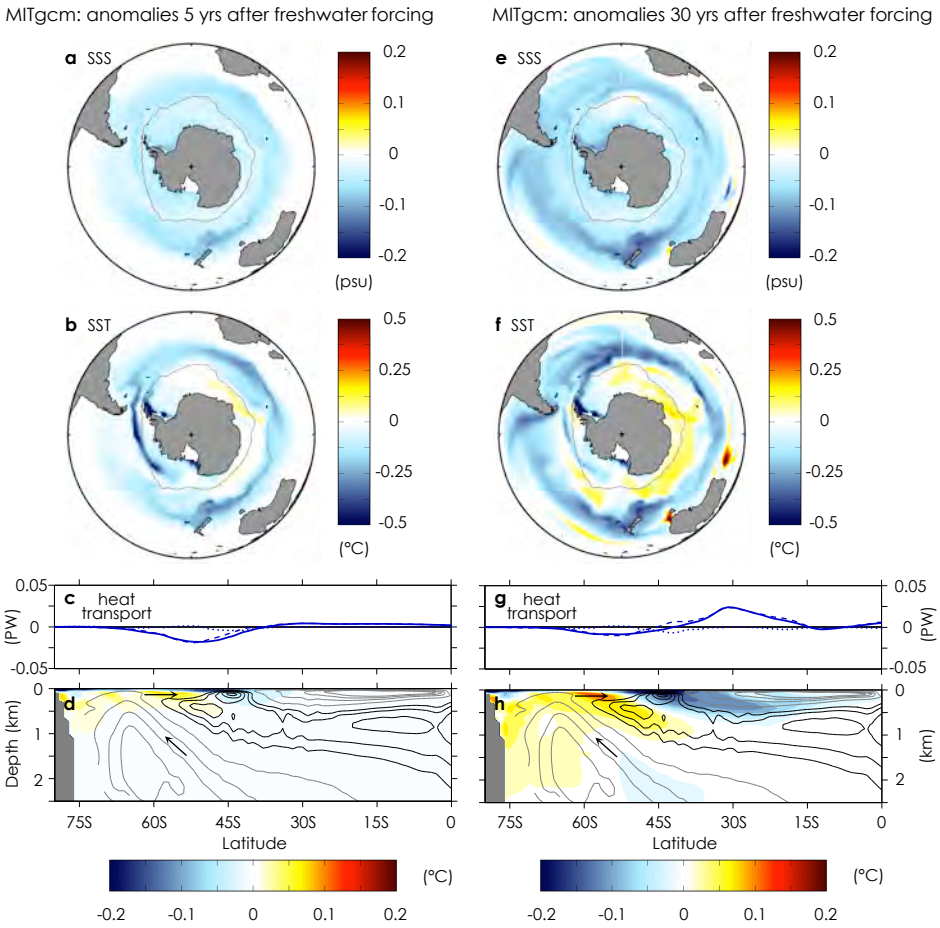

Figure S13. MITgcm response to abrupt freshwater forcing after 5 yrs (left) and after 30 yrs (right). a, Annual-mean sea-surface salinity anomaly; **b,** Annual-mean sea-surface temperature anomaly; **c,** Anomalous OHT (solid, dashed and dotted lines show total, residual-mean advection, and diffusion, respectively); **d,** Zonal-mean ocean potential temperature anomaly, with contours showing the MOC from the control simulation (black contours show positive circulation in 2 Sv increments, gray contours show negative circulation in -4 Sv increments); **e-h,** As in **a-d**, but at yr 30. Grey line in **a,b,e,f** shows maximum winter sea-ice extent, as in Fig. 1 of the main text.

Comparing the MITgcm response to individual forcings. To evaluate the role of individual forcings in delayed SO warming, we quantify the impact of each on the difference between the SST anomaly averaged south of 50°S and the global-mean SST anomaly (D, as defined above). Figure S14a shows the value of D following each abrupt forcing – GHG as in the main text, and westerly wind and freshwater as above. Westerly wind forcing drives an initial cooling of the SO (and negative D), but warming of the SO (and positive D) beyond a couple decades. Freshwater forcing drives an initial cooling of the SO (negative D), but the value of D diminishes within a few decades as the surface temperature anomaly is advected northward across the ACC. Meanwhile, GHG forcing drives a strong decrease in D as the global sea-surface warms far more quickly than the SO south of 50°S.

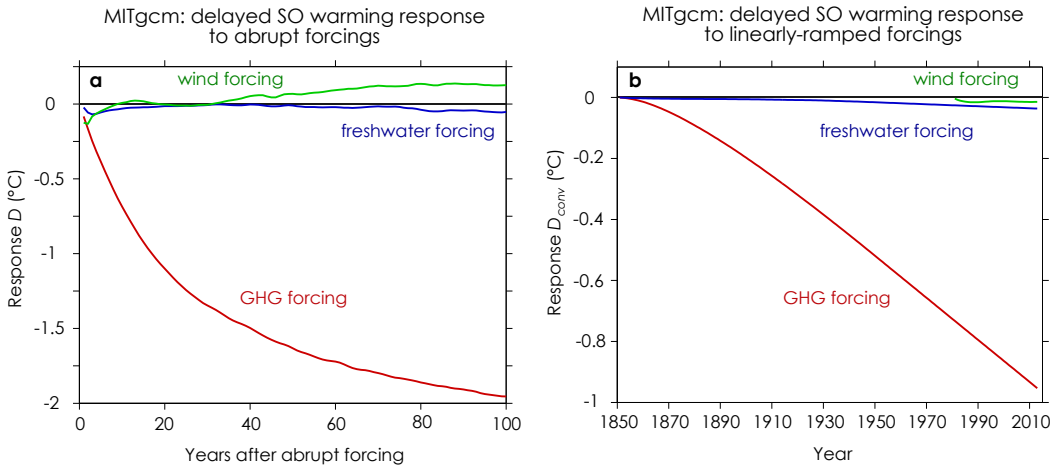

Figure S14. MITgcm delayed SO warming response to GHG, wind and freshwater forcing. a, Response to abrupt forcings; **b,** Response to linearly-ramped forcings calculated with equation (2).

We can further compare the extent to which each forcing has driven trends in D over the historical period by convolving the responses to each abrupt forcing, shown in Fig. S14a, with trends in forcing since pre-industrial. In particular, we estimate the response for each forcing as:

$$D_{conv}(t) = \int_0^t D(t-\tau)\frac{\partial F}{\partial t}(\tau)d\tau, \tag{2}$$

where F is the prescribed forcing timeseries and we have assumed that the response to each forcing scales linearly with its magnitude.

For simplicity, we assume each forcing ramps linearly over time: we prescribe GHG forcing to increase linearly to 2.3 Wm^{-2} over 1850 to 2012, based on the best estimate of the present global-mean radiative forcing[24]; we prescribe freshwater forcing anomaly over the SO to increase linearly to 0.15 mm/day over 1850 to 2012, based on the change in P-E in CMIP5 models[23]; and we prescribe westerly wind forcing to increase linearly by one standard devotion in the SAM over 1980 to 2012, based on observed changes in SAM over the period[25]. Figure S14b shows the delayed SO warming response (D_{conv}) to each forcing. GHG forcing produces a strong decrease in D over the historical period, with a trend of $-0.07°$/decade over 1950-2012; this is very similar to the observed trend in D of $-0.06°$/decade over 1950-2012 (Fig. S8). Wind and freshwater forcing each contribute to delayed SO warming, but at a much reduced degree relative to GHG forcing. This can be understood from the responses to each abrupt forcing (Fig. S14a) which show that only with the first few years is the magnitude of delayed SO warming induced by wind and freshwater comparable to that of GHG forcing; on decadal to centennial timescales, delayed SO warming is primarily a response to GHG forcing.

1. Smith, T.M., Reynolds, R.W., Peterson, T.C. & Lawrimore, J. Improvements to NOAA's Historical Merged Land–Ocean Temp Analysis (1880-2006). *J. Clim.* **21**, 2283–2296 (2008).

2. Good, S.A., Martin, M.J. & Rayner, N.A. EN4: quality controlled ocean temperature and salinity profiles and monthly objective analyses with uncertainty estimates.*J. Geophys. Res. Oceans*, **118**, 6704–6716 (2013).

3. Gouretski, V., & Reseghetti, F. On depth and temperature biases in bathythermograph data: Development of a new correction scheme based on analysis of a global ocean database. *Deep Sea Res., Part I*, **57**, 812–833 (2010).

4. Levitus, S., Antonov, J.I., Boyer, T.P., Locarnini, R.A., Garcia, H.E., & Mishonov A.V. Global ocean heat content 1955-2008 in light of recently revealed instrumentation problems, *Geophys. Res. Lett.*, **36**, L07608 (2009).

5. Ishii, M. & Kimoto, M. Reevaluation of historical ocean heat content variations with time-varying XBT and MBT depth bias corrections. *J. Oceanography*, **65(3)**, 287–299 (2009).

6. McDougall, T.J. & Barker, P.M. Getting started with TEOS-10 and the Gibbs Seawater (GSW) Oceanographic Toolbox, 28pp., SCOR/IAPSO WG127, ISBN 978-0-646-55621-5 (2011).

7. Church, J.A., *et. al.* Ocean temperature and salinity contributions to global and regional sea level change. In: Church, J.A., Woodworth, P.L., Aarup T., & Wilson, W.S. (eds) Understanding sea level rise and variability. Blackwell, New York, pp 143–176 (2010).

8. Sutton, P., & Roemmich, D. Decadal steric and sea surface height changes in the Southern Hemisphere. *Geophys. Res. Lett.* **38**, L08604 (2011).

9. Durack, P.J., Gleckler, P.J., Landerer, F.W. & Taylor, K.E. Quantifying underestimates of long-term upper-ocean warming. *Nature Climate Change* **4**, 999–1005 (2014).

10. Storto, A., Dobricic, S., Masina, S. & Di Pietro, P. Assimilating Along-Track Altimetric Observations through Local Hydrostatic Adjustment in a Global Ocean Variational Assimilation System. *Mon. Weather Rev.*, **139**, 738–754 (2011).

11. Balmaseda, M. A., Mogensena, K. & Weaver, A. T. Evaluation of the ECMWF ocean reanalysis system ORAS4. *Q. J. R. Meteorol. Soc.*, **139**, 1132–1161 (2013).

12. Carton, J. A. & Giese, B.S. A Reanalysis of Ocean Climate Using Simple Ocean Data Assimilation (SODA), *Mon. Weather Rev.*, **136**, 2999–3017 (2008).

13. Kohl, A. Evaluation of the GECCO2 Ocean Synthesis: Transports of Volume, Heat and Freshwater in the Atlantic. *Q. J. R. Met. Soc.*, 141(686), 166-181 (2015).

14. Yu, L., X. Jin, and R. A. Weller. Multidecade Global Flux Datasets from the Objectively Analyzed Air-sea Fluxes (OAFlux) Project: Latent and sensible heat fluxes, ocean evaporation, and related surface meteorological variables. Woods Hole Oceanographic Institution, OAFlux Project Technical Report. OA-2008-01, 64pp. Woods Hole. Massachusetts (2008).

15. Zhang, Y.-C., Rossow, W.B., Lacis, A.A., Oinas, V., & Mishchenko, M.I. Calculation of radiative fluxes from the surface to top of atmosphere based on ISCCP and other global data sets: Refinements of the radiative transfer model and the input data. *J. Geophys. Res.*, **109**, D19105 (2004).

16. Kanamitsu, M., et. al. NCEP-DOE AMIP-II Reanalysis (R-2). *Bull. Amer. Met. Soc.*, 1631-1643 (2002).

17. Reynolds, R.W., Rayner, N.A., Smith, T.M., Stokes, D.C. & Wang, W. An improved in situ and satellite SST analysis for climate. *J. Clim.* **15**, 1609–1625 (2002).

18. Berry, D. I. & Kent, E. C. Air-Sea Fluxes from ICOADS: The Construction of a New Gridded Dataset with Uncertainty Estimates. *International Journal of Climatology*, **31(7)**, 987–1001 (2011).

19. Woodruff, S. D., Diaz, H. F., Worley, S. J., Reynolds, R. W., & Lubker, S. J. Early ship observational data and ICOADS. *Climatic Change*, **73**, 169–194 (2005).

20. Large, W. G. & Yeager, S. G. The global climatology of an interannually varying air-sea flux data set. *Clim. Dyn.*, **33**, 341–364, doi:10.1007/s00382-008-0441-3 (2009).

21. Saha, S. *et. al.* The NCEP Climate Forecast System. *J. Climate*, **19**, 3483–3517 (2006).

22. Marshall, J., *et. al.* The ocean's role in polar climate change: asymmetric Arctic and Antarctic responses to greenhouse gas and ozone forcing. *Phil. Trans. R. Soc. A* **372**, 20130040 (2014).

23. Pauling, A.G., Bitz, C.M., Smith I.J. & Langhorne, P. J. The response of the Southern Ocean and Antarctic sea ice to fresh water from ice shelves in an Earth System Model. *J. Clim.*, **29**, 1655–1672 (2016).

24. Myhre, G., *et. al.* Anthropogenic and Natural Radiative Forcing. In: Climate Change 2013: The Physical Science Basis. Contribution of Working Group I to the Fifth Assessment Report of the Intergovernmental Panel on Climate Change [Stocker, *et. al.* (eds.)]. Cambridge University Press, Cambridge, United Kingdom and New York, NY, USA (2013).

25. Christensen, J.H., *et. al.* Climate Phenomena and their Relevance for Future Regional Climate Change. In: Climate Change 2013: The Physical Science Basis. Contribution of Working Group I to the Fifth Assessment Report of the Intergovernmental Panel on Climate Change [Stocker, T.F., *et. al.* (eds.)]. Cambridge University Press, Cambridge, United Kingdom and New York, NY, USA (2013).